High-resolution MR of the intraparotid facial nerve and parotid duct.

T Dailiana, D Chakeres, P Schmalbrock, P Williams and A Aletras

AJNR Am J Neuroradiol 1997, 18 (1) 165-172
http://www.ajnr.org/content/18/1/165

High-Resolution MR of the Intraparotid Facial Nerve and Parotid Duct

Theodora Dailiana, Donald Chakeres, Petra Schmalbrock, Phil Williams, and Anthony Aletras

PURPOSE: To describe a high-resolution MR imaging technique that depicts the complex anatomy of the region of the parotid gland, focusing on the intraparotid components of the facial nerve and parotid duct. **METHODS:** High-resolution T1-weighted images of the parotid gland were acquired with a prototype three-dimensional Fourier transform gradient-echo sequence that permits a very short echo time (4.2 milliseconds) by using a modified phase-encoded time-reduced acquisition scheme. The sequences were obtained at 1.5 T with a head and neck coil. Postprocessed multiplanar, curved and volumetric images were obtained. The most clinically useful images were acquired at parameters of 30/4.2 (TR/TE_{eff}) a flip angle of 30°, a field of view of 18 to 20 cm, a matrix of 512 × 288 or 512 × 256, an axial plane, 60 images, no gaps, and a section thickness of 1.5 mm. Eighteen healthy subjects were examined. The position of the facial nerve within the parotid gland was determined by identifying the facial nerve in the stylomastoid foramen and then following it on sequential sections through the parotid gland. Curved reformations were used to confirm the visibility of the nerve. A similar technique was used for the parotid duct. **RESULTS:** The image contrast obtained was similar to that of standard spin-echo T1-weighted images. The parotid gland showed intermediate signal intensity while the fat spaces showed high signal signal intensity. The vessels had variable signal intensity depending on saturation. The cerebrospinal fluid, nerves, muscles, and ducts had lower signal intensity. In all 18 subjects, the facial nerve from the brain stem to the parotid gland, and the parotid duct from the mouth to the hilus of the gland were seen bilaterally. The proximal intraparotid facial nerve to the level of the retromandibular vein was seen in 72% of the subjects and the main intraparotid ducts were seen in 66% of the subjects. **CONCLUSION:** High-resolution MR imaging offers simultaneous display of most of the important structures in the region of the parotid gland, including the intraparotid duct and facial nerve.

Index terms: Salivary glands, anatomy; Salivary glands, magnetic resonance

AJNR Am J Neuroradiol 18:165–172, January 1997

With the development of microsurgical techniques for the head and neck area, improved imaging, which allows three-dimensional views of small structures, is becoming more important for successful diagnosis and treatment. We present a high-resolution imaging technique for examining the region of the parotid gland and adjacent structures that can portray the normal anatomy in detail and show the exact relationships of structures, which, although traditionally discrete in pictures of anatomic specimens, have not been displayed clearly on routine magnetic resonance (MR) imaging studies (1, 2). The region of the parotid gland is challenging because of its complex anatomy and the potential serious surgical complications associated with injuries to the facial nerve, parotid duct, and vessels. In the past, surgical exploration was necessary to evaluate accurately the relationship of the abnormalities to the structures of this area.

Our goal was to develop a clinically feasible high-resolution MR imaging technique that would routinely portray the anatomy of the parotid region, including the intraparotid facial nerve and salivary ducts (3 to 5).

Received June 2, 1995; accepted after revision July 5, 1996.

Supported in part by research grant R29DC01646 from the National Institute for Deafness and Other Communication Disorders, National Institutes of Health, Bethesda, Md.

From the Department of Radiology, The Ohio State University College of Medicine, Ohio State University Hospital, S-209 Rhodes Hall, 410 W 10th Ave, Columbus, OH 43210. Address reprint requests to Donald Chakeres, MD.

AJNR 18:165–172, Jan 1997 0195-6108/97/1801–0165

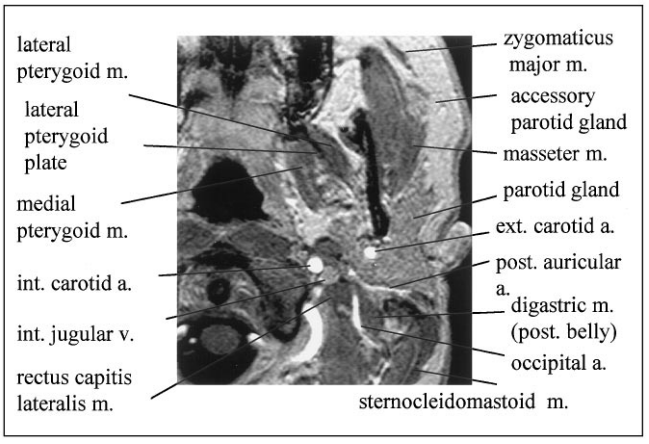

Fig 1. Axial MR image (30/4.2) acquired with a flip angle of 30°, and FOV of 20 cm, section thickness of 1.5, and a 60-section acquisition. The parotid gland appears as a polylobulated, intermediate signal structure. The parotid gland's posterior margin is delineated at this level by the high-signal posterior auricular artery. The accessory parotid gland is seen lateral to the masseter muscle, in the course of the parotid duct. The internal and external carotid, occipital, and vertebral arteries have high signal intensity caused by time-of-flight effects.

Materials and Methods

High-resolution MR images of the parotid gland region were acquired with a prototype three-dimensional Fourier transform (3DFT) gradient-echo sequence that allows a very short echo time (TE) (Figs 1–9). In this sequence, TE shortening was achieved by using a modified stepping scheme for the phase-encoded gradients (both in the plane and along the section-encoding direction) (6). Short phase-encoded gradients were used for the portion of the data acquisition that determines the contrast (ie, the central portion of k-space) and longer gradients were used for the remaining portions. To optimize the image contrast, 15 volunteers were initially studied with various techniques, including gradient-recalled acquisition in the steady state (GRASS) or the spoiled GRASS sequences, with several different flip angles (20 to 60°) and repetition times (TRs) (33 to 17 milliseconds), and with either prototype bilateral phased-array surface coils (7), a routine head coil (General Electric, Milwaukee, Wis), or a movable head and neck coil (Medical Advances, Wawatosa, Wis). In addition to these studies, computer simulations were carried out using the equations given by Meulen et al (8) to aid the selection of optimal parameters and to provide a more general picture of the contrast behavior of the two sequence types at different flip angles and TR. For the computer simulations, we used T1/T2 of 2000/1000 for cerebrospinal fluid, 650/70 for brain (9), 800/35 for muscle, and 300/80 for adipose (10).

Using the optimal technique on a 1.5-T imaging unit, we studied 18 healthy subjects (23 to 58 years old) who had no known parotid disease. The optimal technique for routine clinical imaging was in the axial plane with a movable head and neck coil, 3-D GRASS technique with parameters of 30/4.2/1 (TR/effective TE/excitations), a flip angle of 30°, a field of view (FOV) of 18 to 20 cm, a matrix of 512 × 288, a section thickness of 1.5 mm, no gaps, and 60 sections. The acquisition time was approximately 9 minutes. Multiplanar (orthogonal, oblique, and curved) and volumetric reconstruction images of the 3-D data were made using the standard reformation software on the imager and an image workstation (General Electric Advantage Windows) with graphic prescription. The images were compared with textbook anatomic sections and diagrams.

The extracranial facial nerve (ie, in the stylomastoid foramen) was seen as a low-signal linear structure surrounded by fat (Figs 3 and 4). The most proximal extracranial extraparotid segment was seen in all healthy subjects (Fig 3). Other small, low-signal structures were occasionally seen near the stylomastoid foramen, but they did not course into the gland and were continuous with adjacent vascular structures.

The position of the facial nerve within the posterosuperior portion of the parotid gland was determined by identifying the facial nerve in the stylomastoid foramen and then following it on sequential sections through the parotid gland (Figs 3, 4, 7, and 8). A curved reformatted image along the nerve was used to follow this identified structure. This reformatted image confirmed the identity and continuity of the facial nerve by showing its characteristic curved extension from the stylomastoid foramen into the posterosuperior segment of the parotid gland. Occasionally, an appropriate branching pattern was seen as the nerve divided into its separate segments.

The low-signal-intensity parotid duct surrounded by high-signal-intensity fat was reviewed in a similar fashion. The duct from the mouth to the hilum of the parotid gland

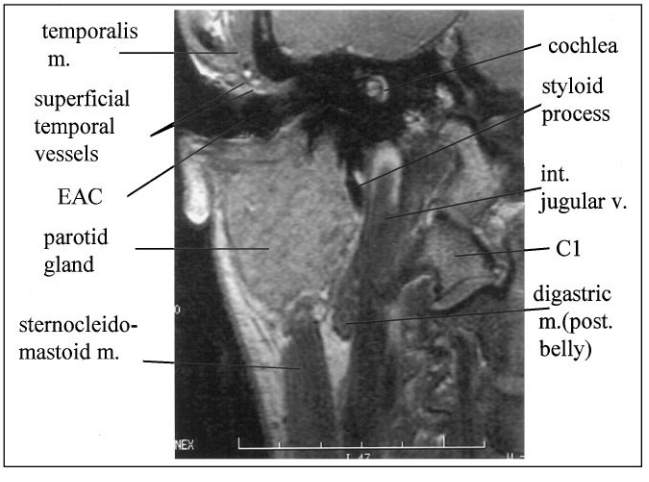

Fig 2. Coronal MR image at the level of the external auditory canal (*EAC*). The gland has an inverted triangular configuration. Its superior margin is formed by the external auditory canal and temporal bone. The lateral margin is the pinna and subcutaneous tissues. Medially, the parotid gland borders the styloid process, internal jugular vein, and posterior belly of the digastric muscle. Other labeled structures include the cochlea, temporalis muscle, superficial temporal vessels, the lateral mass of the first cervical vertebrae (C1), and the styloid process.

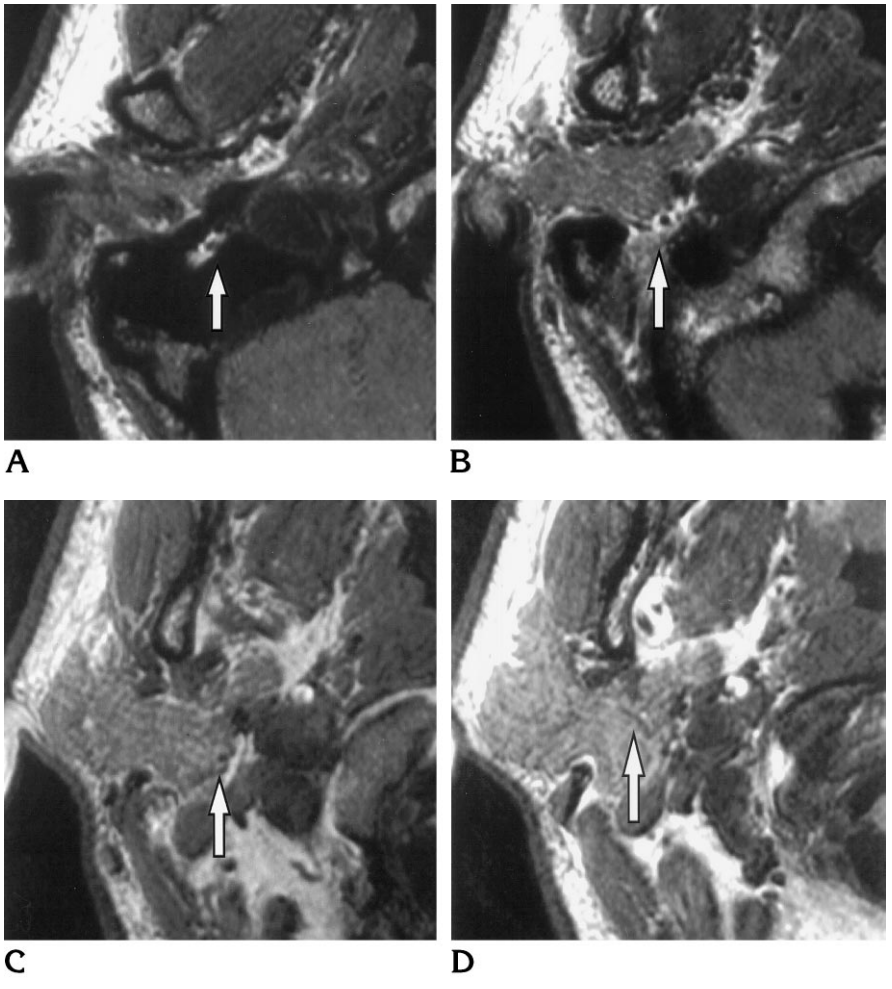

Fig 3. Noncontiguous axial MR images of the proximal extracranial parotid facial nerve. *A* is most superior and *D* is most inferior. The facial nerve (*arrow*) is seen as a low-signal structure surrounded by fat in the stylomastoid foramen (*A*) in its extracranial segment posterior to the parotid gland (*B*). *C* shows the facial nerve (low signal just anterior to *arrow*) just entering the posterosuperior segment of the parotid gland. A small, low-signal, linear blood vessel is visible just lateral to the nerve. Note that the vessel does not enter the gland but courses posteriorly and laterally in the opposite direction from the facial nerve (*C*). *D* illustrates the typical appearance of the facial nerve (*arrow*) in the gland, as a low-signal structure extending anteriorly and laterally toward the posterior margin of the retromandibular vein.

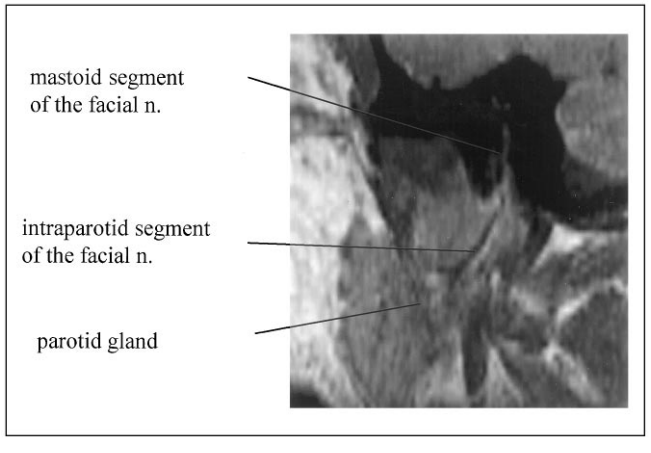

Fig 4. Curved sagittal reconstruction of the descending and intraparotid facial nerve is a reformation from multiple axial images (Fig 3). The plan of sections curves along the course of the nerve, producing a sagittal appearance. The mastoid segment is clearly connected to the intraparotid segment. Distal branching of the facial nerve was not commonly seen, but is visible in this example.

could be followed on a few axial images (Fig 5). The continuation of the duct into the anteroinferior gland was followed with a curved reconstruction to confirm its position (Figs 6–8). The frequency with which the intraparotid facial nerve and duct were seen was determined.

Results

Predominantly axial 3DFT images were obtained (Fig 1). Occasionally, coronal (Fig 2) and, rarely, sagittal primary data sets were acquired. They all provided very good information about the morphology of the examined structures, but the axial images were the most useful for reconstructions and routine clinical use. Curved sagittal reconstructions optimally showed the course of the facial nerve (Figs 4, 7, and 8). A similar display of the parotid duct and its rami was obtained by using curved sagittal reconstructions. Volume surface reconstructions could also be used to display the anatomy (Figs 6 and 9). Oblique reconstructions allowed

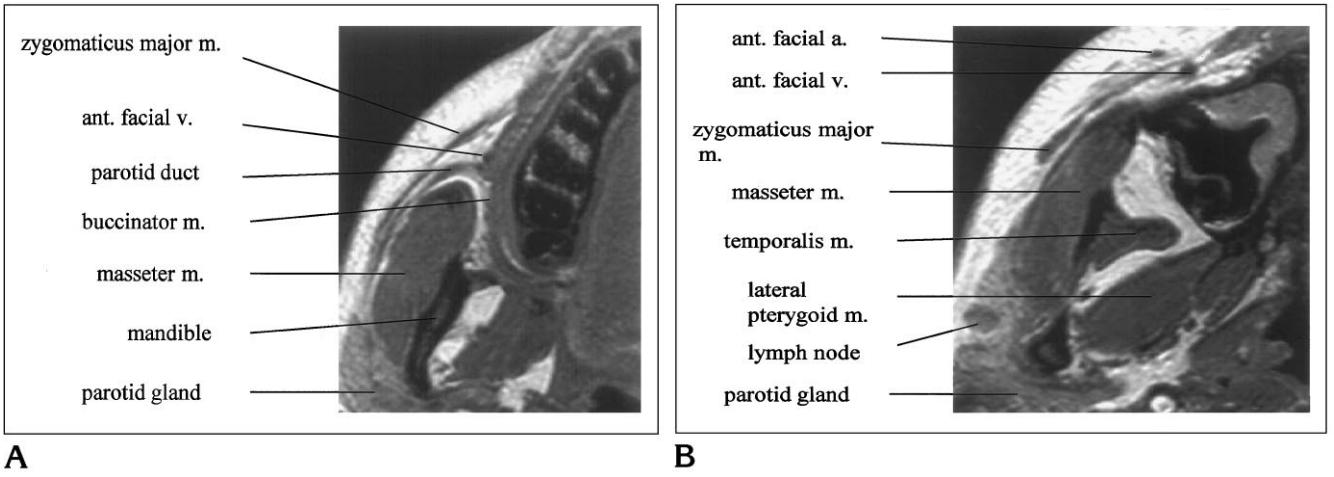

Fig 5. Axial MR images through Stensen's duct.

A, The parotid duct (Stensen's duct) is seen as it penetrates the buccinator muscle just lateral to the second molar. The teeth in the maxillary alveolar ridge are seen just medial to the buccinator muscle. The anterior facial vein is between the duct and the muscle.

B, The course of the zygomaticus major muscle is seen at a slightly more superior level.

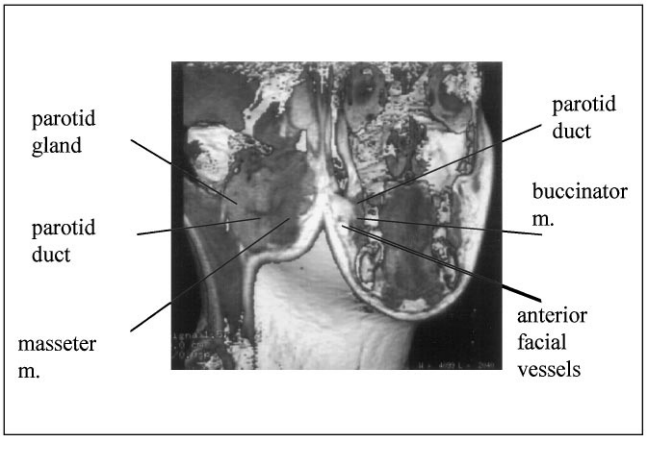

Fig 6. Surface and section plane volume image of the parotid duct and its intraparotid duct rami is a reconstruction of a 120-section acquisition. The head is viewed from a 45° right lateral perspective. The anterior surface is along the coronal plane through the orbits, maxillary sinuses, and mouth. The parotid duct crosses the face to penetrate the buccinator muscle just superior to the facial vessels. The lateral cut surface is through the masseter muscle and parotid gland, showing the internal ductal branching pattern. The branches divide at almost 90°.

complete visualization of the small muscles of this region.

Normal parotid gland tissue showed an intermediate signal intensity (higher than muscle and lower than fat) and a characteristic fine lobular margin (Figs 1–3). No capsular or fascial division of the deep and superficial portions of the parotid gland was seen. Stensen's duct appeared as a low-signal linear structure surrounded by buccal fat and measuring 2 to 3 mm in diameter (Figs 5–8). The duct could be seen lateral to the masseter muscle and medial to the zygomaticus major muscle, finally penetrating the buccinator muscle in a location consistently posterior to the anterior facial vein. The duct was frequently in close approximation to the lateral margin of the masseter muscle just before entering the gland. The segment of the duct from the oral cavity to the hilum was seen in all cases. The parotid duct was often accompanied by a small nodular structure of intermediate signal (similar to the gland), representing an accessory parotid gland (Fig 1).

Intraparotid ducts could be seen in 66% of the glands, with a characteristic wide-angle branching pattern of approximately 80° (Figs 6–8) when visible. The intraparotid ducts were seen bilaterally when visible. The largest ducts were seen at the hilum of the gland, which is in the anteroinferior segment lateral and anterior to the retromandibular vein. The intraparotid facial nerve could also be seen in 72% of healthy subjects from the posterosuperior aspect of the gland to approximately the level of the retromandibular vein (Figs 3, 4, 7, and 8). In those patients in whom the intraparotid facial nerve could be seen, the nerve did not branch early.

The regions of visibility of the intraparotid facial nerve and the intraparotid ducts were in two distinctly separate segments of the gland, so that confusion between the two did not occur (Fig 8). The intraparotid configuration of the ducts and nerves was also completely different.

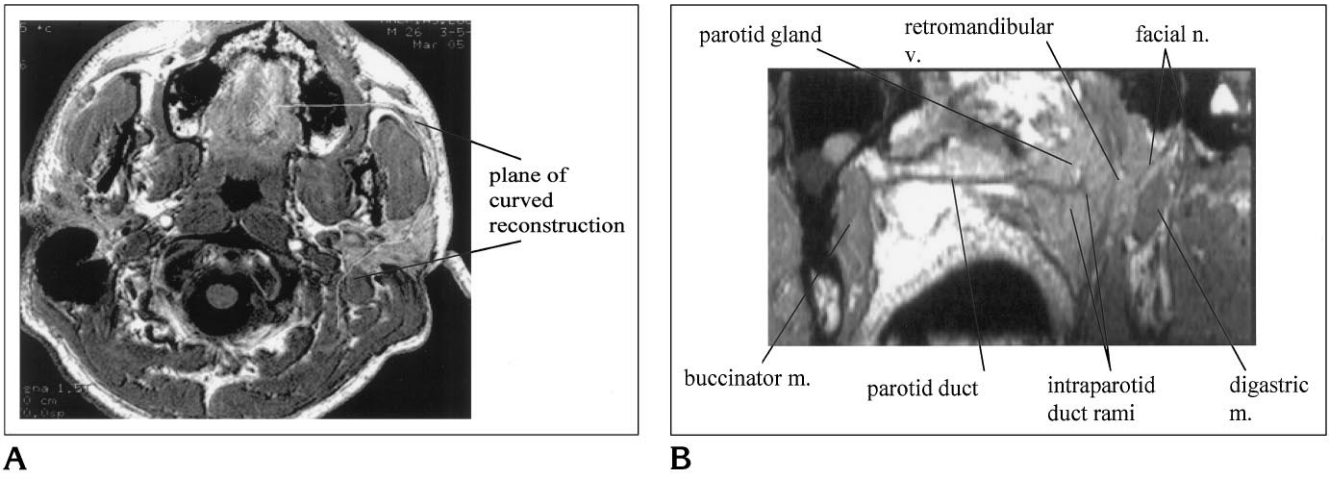

Fig 7. Curved sagittal reconstructions along the facial nerve and the parotid duct.

A, Axial section shows the plane of the curved reconstruction that follows the course of the facial nerve posteriorly (descending through the posterosuperior segment of the parotid gland) and the parotid duct and intraparotid ducts anteriorly.

B, In this curved sagittal reconstruction, the parotid duct is visible from the oral cavity to the intraparotid ducts. Note the characteristic pattern of the parotid ducts, with almost 90° branches. The intraparotid retromandibular vein appears as a vertical low-signal region as a result of saturation. The facial nerve in the temporal bone and parotid is seen in continuity.

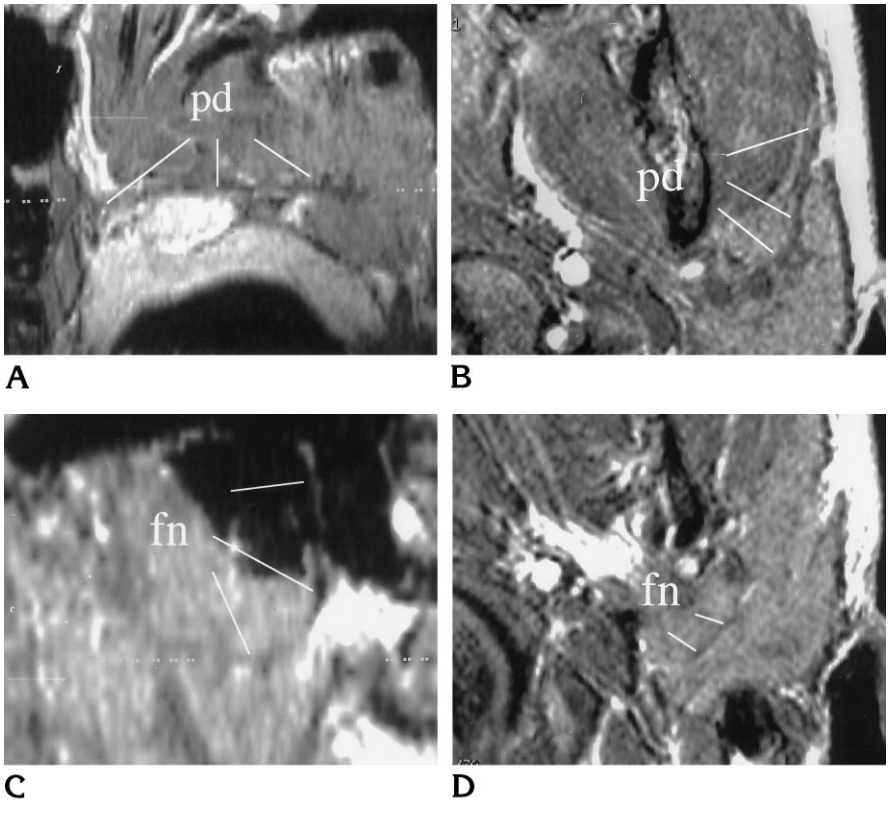

Fig 8. Curved reconstructions and original axial MR images of the intraparotid facial nerve and parotid duct. All images are from a single 3-D acquisition.

A, Curved sagittal reconstruction parallel to the left partoid duct (*pd*). The main intraparotid duct is visible with small branches. The *dotted line* is parallel to the section plane of *B*.

B, Original axial image, parallel to the duct, shows its anterior and inferior location in the hilus of the gland. The parotid duct is seen exiting the gland anteriorly.

C, Curved sagittal reconstruction parallel to the facial nerve (*fn*). The *dotted white line* is parallel to the image plane of *D*.

D, Original axial section shows the horizontal portion of the facial nerve (*fn*) in the posterosuperior segment of the gland. The facial nerve and parotid duct are seen in two distinctly different portions of the gland. They have characteristic appearances and cannot be confused.

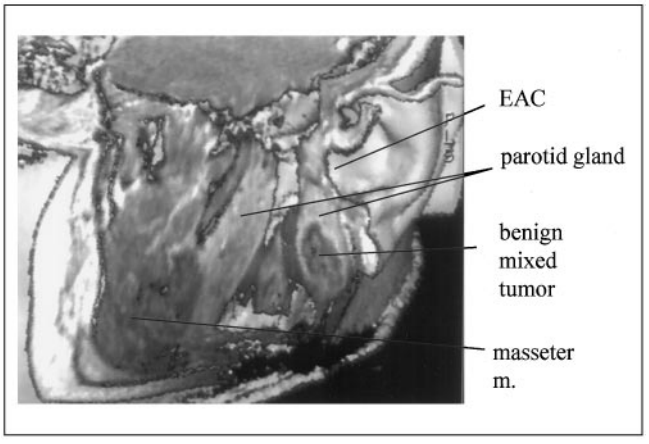

Fig 9. Surface and section volume view of a benign parotid tumor is a volume reconstruction from an axial image acquisition. The left side of the face is viewed from a left anterior oblique angle. A rectangular section has been removed, exposing the sagittal and coronal planes. The surface of the pinna and external auditory canal (*EAC*) are well seen. This 55-year-old patient had a benign mixed tumor, which is lower in signal intensity than the normal gland. It is seen as an oval mass just inferior to the pinna, producing a bulge on the lateral skin surface. Other labeled structures include the masseter muscle and the normal parotid gland.

In some healthy subjects, the ducts could be seen but not the facial nerve, and vice versa.

Owing to blood flow and the location of the image volume, the arteries had high signal intensity when not saturated (Fig 1). There could be extensive saturation and low signal intensity of the vessels. The signal of the venous structures was predominantly suppressed because of saturation, except in entry zone sections (Fig 2). Although flow-compensating gradients were not used, no major flow artifacts were observed. A few flow-related artifacts were sometimes observed in the carotid arteries, but smaller arteries were not affected at all. The inferior internal carotid and most of the external carotid artery and its branches (posterior auricular, anterior facial, internal maxillary, superficial temporal) as well as the internal and external jugular vein and its tributaries (superficial temporal, retromandibular, anterior facial) were followed throughout their course, and their relationship with the adjacent structures was displayed. Small arterial branches near the stylomastoid foramen were occasionally seen. These were not confused with the intraparotid facial nerve, because they coursed from anterior to posterior as they went posteriorly, which is opposite to the course of the facial nerve. These vessels also did not enter the parotid gland.

The muscles showed low to intermediate signal intensity (higher than the fluid and lower than the gland) (Figs 1, 2, and 5). Oblique reconstructions allowed routine visualization of the complete course of the sternocleidomastoid, posterior belly of the digastric, styloglossus, stylohyoid, stylopharyngeous, medial and lateral pterygoid, masseter, temporalis, buccinator, and zygomaticus major muscles.

Discussion

A complete examination of the parotid gland region has required a combination of sialography, angiography, and either computed tomography (CT) or MR imaging. After multiple studies, the radiologist must fuse the information obtained from the separate imaging techniques. Even with multiple examinations, many important structures are not clearly delineated, such as the position of the facial nerve or the relationship of the various structures to one another. Because of relatively rapid saturation and slow flow of these small vessels, it has been difficult to follow then over long distances or to create routine MR angiographic images. The angiographic information provided by the technique described here is important, since the detailed anatomy of the venous and arterial structures is seen along with the relationship of these structures to the other parotid components.

Since the data are in a 3-D format, surface and volume reconstructions are possible for direct comparison with the findings at physical examination and for use in possible surgical interventions (Figs 6 and 9). Because of the versatility of this type of examination, it may, in fact, be less expensive than a combination of other procedures.

Several technical factors need to be optimized in order to produce high-quality images. The phased-array coils generate the highest signal-to-noise ratio peripherally, but because of the signal drop-off they are difficult to postprocess. They are also less versatile for examining deep structures and are more difficult to set up. The movable volume head and neck coil has a signal-to-noise advantage of up to 50% compared with the head coil. This difference in signal-to-noise ratio is important for depicting the many small structures. The neck coil could be centered lower over the mandible and the face, making it suitable for most studies.

In our study, optimal results were achieved with an FOV of 20 cm, a 512 $\times$ 288 matrix, a

Expected signal-to-noise ratio (SNR) based on spatial resolution (for constant TR/TE of 30/4.2, flip angle of 30°, and bandwidth of 16 kHz)

Field of View, cm	Matrix	Section Thickness	No. of Sections	SNR	Voxel, mm^3	Scan Time, min
20	512 × 256	1.5	60	1	0.39 × 0.76* × 1.5	8:20
20	512 × 288	1.5	60	0.94	0.39 × 0.69* × 1.5	9:20
18	512 × 256	1.5	60	0.80	0.35 × 0.7* × 1.5	8:20
18	512 × 288	1.5	60	0.76	0.35 × 0.63* × 1.5	9:20
20	512 × 256	1.5	28	0.71	0.39 × 0.7* × 1.5	4:10
20	512 × 256	0.7	60	0.47	0.39 × 0.7* × 0.7	8:20
20	512 × 256	1.5	124†	1.41	0.39 × 0.7* × 1.5	16:40
20	512 × 256	1.5	124‡	1*f(TR)	0.39 × 0.7* × 1.5	9:30
20	512 × 512	1.5	60	0.71	0.39 × 0.35 × 1.5	16:40
20	512 × 384	1.5	60	0.82	0.39 × 0.52* × 1.5	12:20
22	512 × 512	1.5	60	0.86	0.43 × 0.43 × 1.5	16:40
22	512 × 384	1.5	60	0.99	0.43 × 0.57* × 1.5	12:20
24	512 × 512	1.5	60	1.02	0.47 × 0.47 × 1.5	16:40
24	512 × 384	1.5	60	1.17	0.47 ×0.63* × 1.5	12:20

* Interpolated to square smaller pixel size in plane.

† Assuming TR = 30 ms, bandwidth = 16 kHz.

‡ Assuming TR = 17 ms, bandwidth = 32 kHz; f(TR) indicates factor for signal loss for shorter TR.

1.5-mm section thickness, and 3-D volume acquisition of 60 sections using the volume head and neck coil. This FOV and matrix size corresponds to an in-plane pixel resolution of 0.39 × 0.69 mm^2. The apparent (effective) resolution in the phase-encoding direction is further increased, since the data are interpolated to a pixel resolution of 0.39 × 0.39 mm^2 (by zero filling the raw time domain data before applying the Fourier transform along the phase-encoding direction).

We attempted to increase the spatial resolution further by reducing the FOV, increasing the matrix size, or decreasing the section thickness. However, with the head coil or the volume neck coil, the resulting decrease in signal-to-noise ratio (Table) led to unacceptable loss of image quality in all cases. Increased matrix sizes not only lead to decreased signal-to-noise ratio but also to prohibitive scan times. Somewhat higher spatial resolution can be achieved in peripheral regions with the phased-array coils, although at the expense of large variations in signal. Excessive scan times are a hindrance for acquisition of 124 image sections when using a TR of 30 milliseconds with a bandwidth to 16 kHz. Acquisition of 120 image sections is possible, however, with a TR of 17 milliseconds and a 32-kHz bandwidth, which leads to more realistic scan times.

In standard gradient-echo sequences, the TE is limited by the duration of the phase-encode gradients for submillimeter spatial resolution. Thus, for the spatial resolution used in this study, standard sequences required a minimal TE of 6 to 8 milliseconds. At this TE and field strength, the signal of fat and water spins are out of phase, leading to low signal on gradient echoes in all voxels that contain water and lipid components. This is a serious problem for the head and neck region that is not a problem in the brain, since there are no fat-water interfaces. The novel phase-encode, time-reduced acquisition technique used in this study permits the acquisition of fat/water in-phase images with standard gradients for the center of k-space without the need of expensive hardware upgrades. Since the center of the k-space largely controls the contrast, the image appears to have an effective short TE. In particular, for imaging in the region of the parotid gland, it is crucial to avoid low-signal linear artifacts that result in out-of-phase TE (6 to 7 milliseconds) of all voxels containing both fat and water at 1.5 T.

For the tissues in the head and neck (muscle, neural tissue, adipose, and cerebrospinal fluid), the GRASS sequence results in higher signal. This is especially pronounced for very short TR; that is, while the signal decreases only slowly with TR on the GRASS images, a significant signal reduction occurs in spoiled GRASS images acquired with a very short TR (17 milliseconds). Furthermore, the contrast between muscle, neural tissue, and fat does not change significantly between spoiled GRASS and GRASS sequences (the main difference is better gray-white matter differentiation with the

spoiled GRASS technique). Because of this, and since the GRASS signal is, in general, higher, GRASS imaging is preferable for imaging the face and neck.

The contrast between the different tissues is fairly independent of TR. Only the overall signal changes with TR. This is unlike the more customary spin-echo sequences, in which changing the TR leads to significant contrast variation. Since the contrast is not dramatically affected by the choice of TR, scan time can be shortened by using a short TR. However, shorter TR will lead to decreased signal-to-noise ratio. Thus, there is a trade-off between short TR and image resolution. Shorter TR, yielding a lower signal-to-noise ratio, will give good image quality only for lower spatial resolution (Table). Longer TR, resulting in a higher signal-to-noise ratio, will permit higher spatial resolution. Signal intensity and contrast in gradient-echo images also varies with the flip angle. Depending on TR, the highest signal is obtained with flip angles of 10° to 25° on spoiled GRASS images and 20° to 40° on GRASS images. The best contrast is achieved with flip angles of 30° to 40° on GRASS images. For flip angles larger than the peak signal flip angle, the contrast between the different tissue types does not change much with the flip angle.

Disadvantages of the technique include its susceptibility to motion artifacts (a fact that demands cooperation of the patient) and the lack of T2-weighted images, which could be very useful for examining the parotid duct system. An open question is the effectiveness of using presaturation pulses to reduce fat signal.

As far as the internal architecture of the parotid gland is concerned, there has been some controversy about the "black lines" seen in its parenchyma and what they actually represent (branches of the facial nerve, rami of the parotid duct, fascial planes) (11). The first investigators discussing the issue considered these to be branches of the facial nerve; in 1993, a study based essentially on the imaging of a single autopsy specimen after injection of contrast material in the parotid duct concluded that all the low-signal lines seen inside the parotid gland represented rami of the parotid duct and that no branch of the facial nerve was seen (12). Images acquired with this current technique commonly, but not always, accurately depict the intraparotid facial nerve, usually to just posterior of the retromandibular vein. Furthermore, in most cases, low-signal lines seen in the deeper portion of the parotid gland could be connected to the main stem of the facial nerve by using curved reconstructions. The parotid duct was also followed to its intraparotid segment and some of its rami were shown; they were confined in the more anterior and inferior portion of the gland (Figs 7 and 8).

Acknowledgment

We thank Linda Chakeres for editing the manuscript.

References

1. Freling NJM, Molenaar WM, Vermey A, et al. Malignant parotid tumors: clinical use of MR imaging and histologic correlation. *Radiology* 1992;185:691–696
2. Chauduri R, Bingham JB, Crossman JE, Gleeson MJ. Magnetic resonance imaging of the parotid gland using the STIR sequence. *Clin Otolaryngol* 1992;17:211–217
3. Romell LJ, Mancuso AA, Larkin LH, Rarey KE, Mahan PE, Ross MH. *Sectional Anatomy of the Head and Neck with Correlative Diagnostic Imaging*. Philadelphia, Pa: Febiger; 1994:28, 30, 38, 42, 43, 148, 150, 154, 158
4. Lillie JH, Bauer BA. *Sectional Anatomy of the Head and Neck*. New York, NY: Oxford University Press; 1994:35–134
5. Ferner H, Monsen H, ed. *Pernkopt Atlas of Topographical and Applied Human Anatomy*. Philadelphia, Pa: Saunders; 1963;1: 113–120, 125, 140–144, 148, 149
6. Ying K, Schmalbrock P, Clymer BD. Echo time reduction for submillimeter resolution imaging with a 3D phase encode time reduced acquisition method. *Magn Reson Med* 1995;33:82–87
7. Schmalbrock P, Pruski J, Sun L, Rao A, Monroe JW. Phased array RF coils for high resolution MRI of the inner ear and brainstem. *J Comput Assist Tomorg* 1995;19:8–14
8. Meulen P, Groen JP, Tinus AMC, Bruntink G. Fast field echo imaging: an overview and contrast calculations. *Magn Reson Imaging* 1988;6:355–368
9. Schmalbrock P, Chakeres DW, Hacker V, Ying K, Clymer BD. Optimization of submillimeter resolution imaging of the inner ear. *J Magn Reson Imaging* 1992;3:451–459
10. Chakeres DW, Schmalbrock P. *Fundamentals of Magnetic Resonance Imaging*. Baltimore, Md: William & Wilkins; 1992: 212–227
11. McGhee RB Jr, Chakeres DW, Schmalbrock P, Brogan M, Negulesco JA. The extracranial facial nerve: high resolution three dimensional Fourier transform MR imaging. *AJNR Am J Neuroradiol* 1993;14:465–472
12. Thibault F, Halimi P, Bely N, et al. Internal architecture of the parotid gland at MR imaging: facial nerve or ductal system? *Radiology* 1993;188:701–704